PHYSICAL REVIEW B **100**, 144101 (2019)

Crystalline phase transitions and vibrational spectra of silicon up to multiterapascal pressures

R. Paul, S. X. Hu,* and V. V. Karasiev
Laboratory for Laser Energetics, University of Rochester, 250 East River Road Rochester, New York 14623-1299, USA

(Received 5 July 2019; published 9 October 2019)

A composite high-pressure phase diagram for silicon has been predicted for up to 4 TPa. This diagram has been built using a combination of evolutionary algorithm-based structure searches, electronic density functional theory, lattice dynamics of perfect crystals, and anharmonic corrections for the solid state in conjunction with molecular dynamics for evaluating the melt curve. The anharmonic corrections to free energy, arising from both finite-temperature multiphonon interactions and temperature dependence of the lattice axial ratios, play a critical role in properly identifying the solid-solid transition boundaries of the orthorhombic structures. A double hexagonal close-packed structure has been found to be thermodynamically and dynamically stable, sandwiched between the experimentally observed base-centered orthorhombic and hexagonal close-packed structures. In addition, beyond 2.8 TPa, there exists a sequence of face-centered cubic-to-body-centered cubic-to-simple cubic transitions that are accompanied by the localization of electrons in the interstitial spaces between the ions. Supplementing the structural calculations, second- and third-order interatomic force constants were evaluated to compute the phonon vibration modes and linewidths, respectively. This allowed an elaborate analysis of the Raman and infrared spectra for all of the structures of silicon identified so far.

DOI: 10.1103/PhysRevB.100.144101

I. INTRODUCTION

In the past several decades, there has been a sustained effort in the condensed matter and materials science research community to computationally construct comprehensive pressure-temperature-density (P-T-ρ) phase diagrams of pure elements, such as H [1,2], Li [3], Be [4], C [5,6], N [7], Na [8], and Al [9] or compounds such as MgO [10] and SiO_2 [11], encompassing ambient to extreme conditions. The importance of most of these elements or compounds stems from their occurrence in planetary interiors [12] or their application to inertial confinement fusion (ICF) designs [13–15], both of which fall under the umbrella of the emerging field of high-energy-density sciences.

A ubiquitous material like silicon has a plethora of applications [16–18], including the ones mentioned earlier. This had prompted us to investigate a lower-temperature region of the silicon phase diagram hitherto ignored, spanning pressures up to a multi-TPa range. In the design of ICF ablators, moderate-Z material is desired because of the mitigating effect on hot electrons in coronal plasma, which arises because of the two-plasmon-decay instability [15]. As such, ablator material based on silicon can reduce the detrimental effects of parametric instabilities in plasma on direct-drive ICF implosions. Also, in the interiors of many rocky planets, silicon forms the basis of multiple coordination compounds. These compounds play a crucial role in the convection currents in the planetary mantle, where pressure-temperature (P-T) conditions can be up to ~4.7 TPa and ~18 000 K, respectively [19]. However, constructing phase diagrams of molecular crystals is both complicated and computationally intensive, so simplifying the problem to that of construction of binary or ternary phase diagrams using elemental phase diagrams [20] is a step in the right direction.

Existing experimental data on silicon have firmly established a melt curve up to ~35 GPa [21–25] and the existence of the following structures upon compression from ambient conditions along the 300 K isotherm [26]: cubic diamond (Si-I) at 0.0001–12.5 GPa [27–34], β-tin (Si-II) at 8.8–16 GPa [27–34], body-centered orthorhombic *Imma* (Si-XI) at 13–16 GPa [35], simple hexagonal (Si-V) at 14–38 GPa [30–33], base-centered orthorhombic *Cmce* (Si-VI) at 40–42 GPa [36], hexagonal close-packed (Si-VII) at 40–78 GPa [32,34,37], and face-centered cubic (Si-X) at 78–248 GPa [34,37]. All such experimental data are limited to below 250 GPa, beyond which the existence of additional phase transitions were unknown. This has also been accompanied by a large body of cold-curve calculations [26,38–40] and equation-of-state (EOS) studies [41–44].

This work presents the *first-principles* construction of a high-P-T phase diagram of Si up to 4 TPa, which revealed stable phases at multi-TPa conditions. The methodology employed in this work was a combination of different first-principles approaches centered on the use of Mermin's extension of Kohn-Sham density functional theory (DFT) [45,46] and *ab initio* lattice dynamics of perfect crystals. Such a computational effort has already been reported earlier, however, without the melt curve [47] and also lacked the anharmonic corrections that are crucial in establishing an accurate free-energy map $F(P,T)$. This was highlighted previously [48] by the authors who pointed out that the slope of the principal Hugoniot and the orthorhombic phase boundaries are drastically affected if the anharmonicity is taken into account. This paper is an elaboration of this earlier work [48] and also

---

[*] shu@lle.rochester.edu

presents a detailed vibrational spectra analysis that could be of assistance to experimentalists.

This paper is broadly divided into four sections. Section I, the current section, deals with the existing literature on the state of the art when it comes to experimental and computational findings on silicon EOS and phases. Section II details the theory behind the calculations performed in this work, whereas Sec. III lays out the results and provides insights and discussions. Lastly, Sec. IV provides our conclusions and closing remarks.

II. THEORY AND METHODOLOGY

This section details the theory and methodology applied in building the solid-state phase diagram from the cold-curve ($T = 0\,\mathrm{K}$) structures. The flow chart corresponding to this section is shown in Fig. 1. In this paper, *state* refers to either solid or liquid, and *structure* refers to crystalline structures such as face-centered cubic, simple hexagonal, etc., whereas *geometry* refers to the lattice constants (a) and axial ratios (b/a, c/a) for a given structure in solid state. Both state and structure are loosely defined as *phases*. Figure 1(a) shows that a cold-curve structure search using evolutionary algorithms at different pressures, ranging from P_{01} to $P_{\rm end}$, with different number of atoms ($N_{\rm a}$) in a unit cell yields the energetically most favorable (corresponding to least enthalpy) structures Γ whose geometry $\mathbf{u}$ would be a function of pressure. Sections II A and II B detail the theory behind the complete Gibbs free-energy calculations, while Sec. II C details the theory for vibrational transition spectra, namely, the inelastic scattering/Raman spectra and the infrared absorption spectra.

A. Cold-curve equation of state

Once a favorable structure Γ is obtained at a certain pressure, starting from that particular geometry $\mathbf{u}$ (P, $T = 0\,\mathrm{K}$) of the structure Γ, the entire pressure (P) domain can be scanned using the simple transformation matrices,

$$\boldsymbol{\Omega}_{\rm a} = \begin{bmatrix} 1+\varepsilon & 0 & 0 \\ 0 & 1+\varepsilon & 0 \\ 0 & 0 & 1+\varepsilon \end{bmatrix},$$

$$\boldsymbol{\Omega}_{b/a} = \begin{bmatrix} 1+\varepsilon & 0 & 0 \\ 0 & \frac{1}{\sqrt{1+\varepsilon}} & 0 \\ 0 & 0 & 1+\varepsilon \end{bmatrix}, \tag{1}$$

and

$$\boldsymbol{\Omega}_{c/a} = \begin{bmatrix} 1+\varepsilon & 0 & 0 \\ 0 & 1+\varepsilon & 0 \\ 0 & 0 & \frac{1}{\sqrt{1+\varepsilon}} \end{bmatrix},$$

for scaling volume by changing the lattice constant a, the b/a axial ratio, and the c/a axial ratio, respectively (preserving the unit cell volume when using $\boldsymbol{\Omega}_{b/a}$ and $\boldsymbol{\Omega}_{c/a}$). Here, ε is the strain rate and can be used as a controlling parameter in the enthalpy minimization. Eventually, the Gibbs free energy G (P, $T = 0\,\mathrm{K}$) or enthalpy H (P) can be given an analytic form by fitting with an appropriate EOS, such as the augmented stabilized jellium EOS (ASJEOS) [49]:

$$G_{\rm cold}(x) = \frac{a}{x^3}g(x) + \frac{b}{x^2} + \frac{c}{x} + d, \tag{2}$$

with $g(x) = 1 + \alpha(1-x)^4 - \beta(1-x)^5 + \gamma(1-x)^6$ and the volume ratio $x = v/v_0$, v_0 being the volume corresponding to the equilibrium geometry (corresponding to the minima of the EOS). This procedure is shown in Fig. 1(b), where "×" implies matrix multiplication and $G_{\rm analytic}(\Gamma; V)$ refers to the analytic cold-curve EOS fit between a minimum and a maximum volume per atom, i.e., $\{V_{\rm min}, V_{\rm max}\}$ for the optimal axial ratios $\gamma \equiv (b/a, c/a)$ at each pressure.

B. *Ab initio* lattice dynamics: Finite-temperature quasiharmonic formulation

For the purpose of calculating finite-temperature thermodynamic variables, we resort to the use of lattice dynamics. The main goal of such a problem is to solve for the many-body ionic total energy E,

$$\begin{aligned}
E &= U + T \\
&= U^{(0)} + U^{(1)} + U^{(2)} + U^{(3)} + \cdots + T \\
&= U^{(0)} + \frac{1}{1!}\sum_{\iota\kappa}\sum_{x}\Phi_x^{(1)}\Delta r_x(\iota\kappa) \\
&\quad + \frac{1}{2!}\sum_{\iota\kappa}\sum_{\iota'\kappa'}\sum_{xy}\Phi_{xy}^{(2)}(\iota\kappa;\iota'\kappa')\Delta r_x(\iota\kappa)\Delta r_y(\iota'\kappa') \\
&\quad + \frac{1}{3!}\sum_{\iota\kappa}\sum_{\iota'\kappa'}\sum_{\iota''\kappa''}\sum_{xyz}\Phi_{xyz}^{(3)}(\iota\kappa;\iota'\kappa';\iota''\kappa'') \\
&\quad \times \Delta r_x(\iota\kappa)\Delta r_y(\iota'\kappa')\Delta r_z(\iota''\kappa'') + \cdots + T \\
&= U^{(0)} + \frac{1}{1!}\sum_{\iota\kappa}\sum_{x}\left.\frac{\partial U}{\partial r_x(\iota\kappa)}\right|_{r_0}\Delta r_x(\iota\kappa) \\
&\quad + \frac{1}{2!}\sum_{\iota\kappa}\sum_{\iota'\kappa'}\sum_{xy}\left.\frac{\partial^2 U}{\partial r_x(\iota\kappa)\partial r_y(\iota'\kappa')}\right|_{r_0}\Delta r_x(\iota\kappa)\Delta r_y(\iota'\kappa') \\
&\quad + \frac{1}{3!}\sum_{\iota\kappa}\sum_{\iota'\kappa'}\sum_{\iota''\kappa''}\sum_{xyz}\left.\frac{\partial^3 U}{\partial r_x(\iota\kappa)\partial r_y(\iota'\kappa')\partial r_z(\iota''\kappa'')}\right|_{r_0} \\
&\quad \times \Delta r_x(\iota\kappa)\Delta r_y(\iota'\kappa')\Delta r_z(\iota''\kappa'') + \cdots + T,
\end{aligned} \tag{3}$$

where ι,κ, and Δr denote unit cell indices, atomic indices, and atomic displacements from their equilibrium positions r_0, respectively; $U^{(0)} \equiv U_{\rm perf}$ is the nonvibrating/rigid-body potential energy of a perfect crystal, $U^{(1)}$ is zero by definition as $\partial U(\iota\kappa)/\partial r_x(\iota\kappa)|_{r_0} = 0$ at equilibrium position r_0, $U^{(2)} \equiv U_{\rm harm}$ is the harmonic potential energy, and $U^{(3)} \equiv U_{\rm anharm}$ is the anharmonic potential energy; the coefficients of the series expansion $\Phi_x^{(1)}$, $\Phi_{xy}^{(2)}$, and $\Phi_{xyz}^{(3)}$ are the first-, second-, and third-order interatomic force constants, respectively, with indices x, y, z denoting the Cartesian coordinates; and $T = \frac{1}{2}\sum_{\iota\kappa}\sum_x m_\kappa \dot{r}_x^2(\iota\kappa)$ is the atomic kinetic energy. We have used PHONOPY [50,51], which takes in the forces obtained from density functional perturbation theory (DFPT) [52]

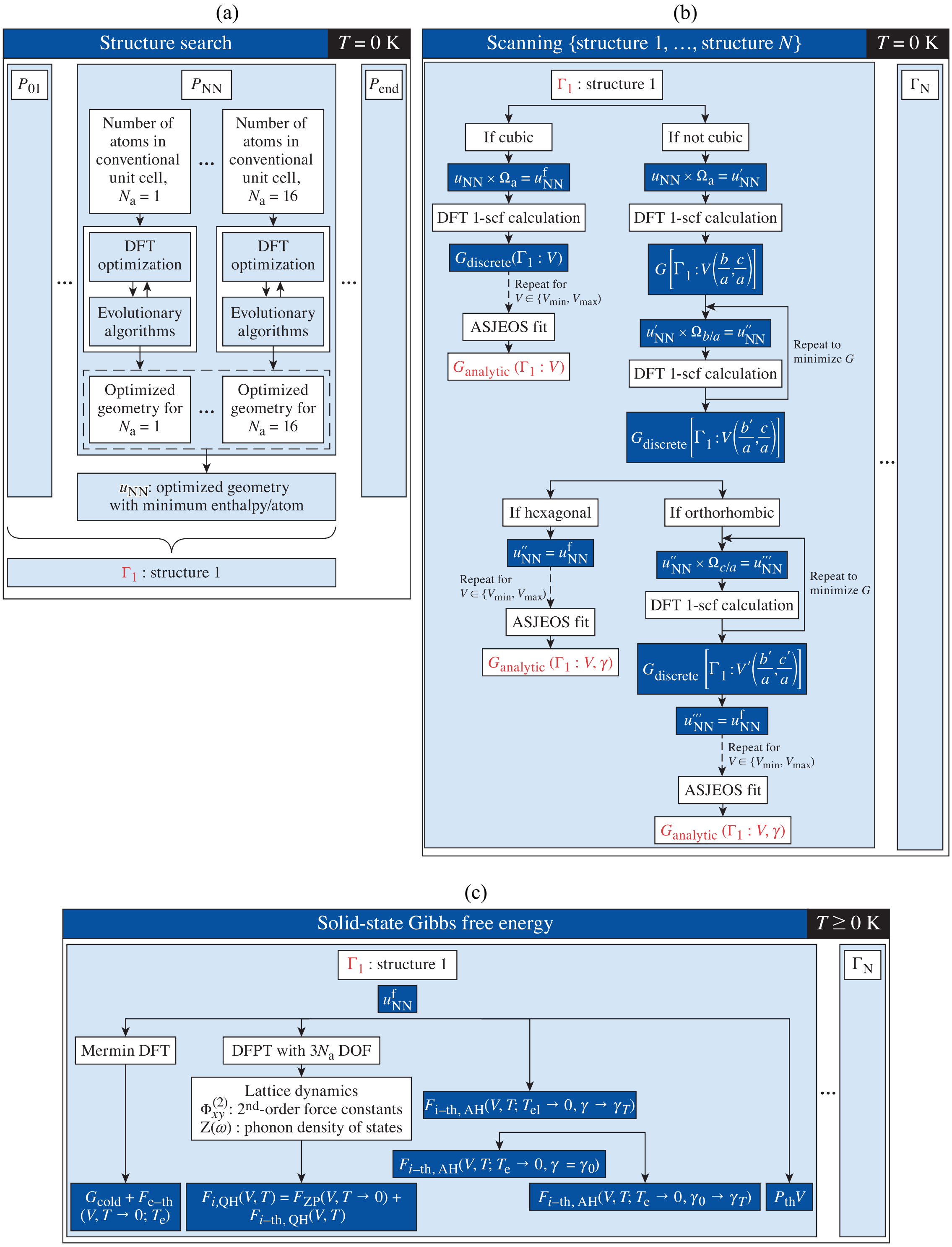

FIG. 1. Flow charts showing the general scheme of methods used, as described in Secs. II A, II B, and II C.

calculations, and computed the harmonic derivatives

$$\Phi^{(2)}_{xy}(\iota\kappa;\iota'\kappa') = \left.\frac{\partial^2 U}{\partial r_x(\iota\kappa)\partial r_y(\iota'\kappa')}\right|_{r_0} = -\left.\frac{\partial F_x(\iota\kappa)}{\partial r_y(\iota'\kappa')}\right|_{r_0} \qquad (4)$$

as $F_x(\iota\kappa) = -\partial U/\partial r_x(\iota\kappa)$ to calculate the second-order force constant $\Phi^{(2)}_{xy}$. The second-order force constant is related to the dynamical matrix/tensor $\mathbf{D}(\mathbf{k})$ as

$$D_{xy}(\kappa\kappa', \mathbf{k}) = \frac{1}{\sqrt{m_\kappa m_{\kappa'}}} \sum_{\iota'} \Phi^{(2)}_{xy}(\iota\kappa;\iota'\kappa') \times \exp[i\mathbf{k} \cdot (r_{0,\iota'\kappa'} - r_{0,\iota\kappa'})], \qquad (5)$$

where m_κ is the mass of atom κ, and $\mathbf{k}$ is the wave vector. Once $\Phi^{(2)}_{xy}$ is known, the dynamical matrix can be accurately determined. Thereafter, we solve the characteristic equation

$$\mathbf{D}(\mathbf{k})\mathbf{W}_{\mathbf{k},\lambda} - \omega^2_{\mathbf{k},\lambda}\mathbf{W}_{\mathbf{k}},_{\lambda} = 0, \tag{6}$$

where $\mathbf{W}_{\mathbf{k},\lambda}$ is the matrix of atomic displacements caused by the traveling wave $\mathbf{k}$ (eigenvectors) and obtain the phonon frequencies ω (from eigenvalues ω^2) of band indices λ.

The phonon spectra, i.e., phonon density of states (PDOS), can be calculated as

$$Z(\omega) = \frac{1}{N_\mathrm{a}}\sum_{\mathbf{k}}\sum_{\lambda}\delta[\omega - \omega_\lambda(\mathbf{k})] \tag{7}$$

for a phonon wave vector $\mathbf{k}$ of band index λ, being normalized such that $\int_0^{\omega_{\max}} Z(\omega)d\omega = 1$, where N_a is the total number of ions. Once the phonon spectra over the first Brillouin zone (1BZ) is obtained from PHONOPY calculations, finite-temperature thermodynamic variables can be obtained via a thermodynamic integration within the quasiharmonic (QH) approximation [only the first and third terms of the expression for total energy in Eq. (3) are considered]. Within the QH approximation, the finite-temperature ionic contribution to the Helmholtz free energy $F_{\mathrm{i,QH}}$ was calculated using

$$\begin{aligned} F_{\mathrm{i,QH}}(V,T) &= F_{\mathrm{ZP}}(V) + F_{\mathrm{i\text{-}th,QH}}(V,T)\\ &= \frac{1}{2}\sum_{\mathbf{k},\lambda}\hbar\omega_\lambda(\mathbf{k},V)\\ &\quad + k_\mathrm{B}T\sum_{\mathbf{k}_\lambda} ln[1 - e^{-\hbar\omega_\lambda(\mathbf{k},V,T)/k_\mathrm{B}T}]. \end{aligned} \tag{8}$$

The first term corresponds to the energy due to the quantum zero-point harmonic oscillations in a perfect crystal that is nonvibrating/rigid, whereas the latter corresponds to the thermal lattice-vibrational free energy above $T = 0\,\mathrm{K}$. In integral form, Eq. (8) becomes

$$\begin{aligned} &F_{\mathrm{i,QH}}(V,T)\\ &\quad = F_{\mathrm{ZP}}(V,T) + F_{\mathrm{i\text{-}th,QH}}(V,T)\\ &\quad = 3N_\mathrm{a}\int_0^{\omega_{\max}}\left[\frac{\hbar\omega}{2} + k_\mathrm{B}T\ln\left(2\sinh\frac{\hbar\omega}{2k_\mathrm{B}T}\right)\right]Z(\omega)d\omega, \end{aligned} \tag{9}$$

where k_B is the Boltzmann constant and $\hbar$ is the reduced Planck constant.

However, this QH approach works only if all the structures have positive vibration frequencies at $T = 0\,\mathrm{K}$, which is not the case for the *Cmce* and *Imma* structures. In such cases of vibrational instability, performing thermodynamic integration relative to the $T = 0\,\mathrm{K}$ system (as a reference system) becomes impossible. Since free energy is a state function and the energy expended in the reversible process while switching from a harmonic to a QH system does not depend on the path followed, any adequate modifications to the harmonic reference system should suffice as long as it is uniformly applied to all the relevant structures. This implies that the reference system should not affect the value of the QH ionic-thermal contribution $F_{\mathrm{i\text{-}th,QH}}$. We employed a methodology similar to the ones employed for Fe [53,54] that uses an inverse power (IP) potential as an additive to the calculated harmonic potential. It should also be noted that merely using an inverse power potential of the form $U_{\mathrm{IP}} = 4A(r/r_0)^{\varphi}$ does not alleviate the said problem for *Cmce*-Si and *Imma*-Si because for $c/a < 1$, as is the case for both *Cmce* and *Imma*, this IP reference system also becomes vibrationally unstable. Therefore, to circumvent this handicap, we did not use an IP potential and resorted to using an Einsteinian potential energy for solids, $U_E = \sum_{\kappa=1}^{N_\mathrm{a}}\frac{1}{2}B\Delta r_\kappa^2$, which is added to the harmonic component of the potential energy, $U^{(2)} \equiv U_{\mathrm{harm}}$. Here, B is a constant ($1.7261\ \mathrm{eV}/\mathrm{\AA}^2$ for *Cmce* and $0.8507\ \mathrm{eV}/\mathrm{\AA}^2$ for *Imma*) that is calibrated in such a way that the imaginary modes in the band structure/imaginary frequencies in the PDOS disappear for both *Cmce* and *Imma*. The added Einsteinian potential makes sure the system has sufficient energy that the imaginary frequency values disappear. However, since it is uniformly added for both the $T = 0\,\mathrm{K}$ and finite-temperature cases, it does not show up in the free-energy difference data. This summarizes the approach used to calculate $F_{\mathrm{i,QH}}$ for vibrationally unstable structures.

C. Anharmonicity

The complete classical anharmonic ionic-thermal contribution $F_{\mathrm{i\text{-}th,AH}}$, with γ_T being the optimal axial ratio for a given state (V, T), was evaluated by breaking it up into two separate components [55]:

$$\begin{aligned} &F_{\mathrm{i\text{-}th,AH}}(V,T;T_\mathrm{e}\to 0,\gamma\to\gamma_\mathrm{T})\\ &\quad = F_{\mathrm{i\text{-}th,AH}}(V,T)^{(1)} + F_{\mathrm{i\text{-}th,AH}}(V,T)^{(2)}\\ &\quad = F_{\mathrm{i\text{-}th,AH}}(V,T;T_\mathrm{e}\to 0,\gamma = \gamma_0)\\ &\qquad + F_{\mathrm{i\text{-}th,AH}}(V,T;T_\mathrm{e}\to 0,\gamma_0\to\gamma_\mathrm{T}), \end{aligned} \tag{10}$$

with T being the ionic temperature and T_e being the electronic temperature. The first component tracks the change in free energy, while moving along an isochore, from $T = 0\,\mathrm{K}$ to some finite temperature keeping the axial ratio γ_0 constant, whereas the second term tracks the free-energy change when the axial ratio is changed from γ_0 to γ_T at that temperature.

For the former component, we used a form of thermodynamic integration that relied on the difference between the internal energy U obtained from quantum molecular dynamics (QMD) simulations and the QH Helmholtz free energy. This is because QMD does not explicitly calculate the ionic entropy. The value of this quantity was evaluated at a reference temperature T_{ref} such that $T_{\mathrm{melt}} > T_{\mathrm{ref}} > \Theta$ (Θ is the Debye temperature) and scaled with respect to that temperature for temperatures below the melting point along an isochore. The mathematical form of the expression is as follows:

$$\begin{aligned} \langle F_{\mathrm{i\text{-}th,AH}}(V,T;T_\mathrm{e}\to 0,\gamma=\gamma_0)\rangle|_V &= \langle F_{\mathrm{i\text{-}th,AH}}(V,T_{\mathrm{ref}};T_\mathrm{e}\to 0,\gamma=\gamma_0)\rangle|_V\frac{T}{T_{\mathrm{ref}}}\\ &\quad - T\int_{T_{\mathrm{ref}}}^{T}\frac{\langle U(T)\rangle_{\mathrm{QMD}} - [U(T)]_{\mathrm{cold+i\text{-}th,QH}} - \frac{d(N_\mathrm{a}-1)}{2}k_\mathrm{B}T}{T^2}\Bigg|_V dT, \end{aligned} \tag{11}$$

where $\langle \cdots \rangle_{\mathrm{QMD}}$ was calculated by averaging in a QMD system in thermal equilibrium and $[\cdots]_{\text{cold+i-th,QH}}$ was obtained from summing the cold-curve and QH calculations, and $d(N_{\mathrm{a}}-1)$ is the total number of internal degrees of freedom. The zero-point energy is not a part of the formulation because atomic motions in QMD follow a classical trajectory. Also, since T_{ref} is chosen as close to the melting point as possible, the unknown term $\langle F_{\text{i-th,AH}}(V, T_{\mathrm{ref}}; T_{\mathrm{e}} \to 0, \gamma = \gamma_0)\rangle|_V$ is negligible, since anharmonicity is quantitatively significant at lower temperatures.

For the latter component in Eq. (10) (originating as a result of the temperature dependence of the axial ratios, especially in cases of the orthorhombic structures), a Taylor expansion, truncated after the second-order term, was employed:

$$\begin{aligned}\delta F_{\text{cold+i-th,tot}}(V,T) &= \frac{\partial}{\partial\gamma}F_{\text{cold+i-th,tot}}(V,T)|_{\gamma_0}\delta\gamma \\ &\quad + \frac{1}{2!}\frac{\partial^2}{\partial\gamma^2}F_{\text{cold+i-th,QH}}(V,T)|_{\gamma_0}(\delta\gamma)^2,\end{aligned} \tag{12}$$

under the assumption that $\partial^2/\partial\gamma^2 F_{\text{i-th,AH}}(V,T)|_{\gamma_0} \approx 0$, which was observed from calculations, where $\delta F_{\text{cold+i-th,tot}}(V,T) = F_{\text{cold+i-th,tot}}(\gamma, V, T)$-$F_{\text{cold+i-th,tot}}(\gamma_0, V, T)$, $\delta\gamma = \gamma - \gamma_0$, and the notation i-th, tot[$\equiv$ i-th, QH + i-th, AH] denotes the sum of the QH and anharmonic free energies, where "cold" denotes the cold-curve (electronic) free energy. Differentiating Eq. (11) with respect to $\delta\gamma$ and evaluating at $\gamma = \gamma_T$ with $\partial/\partial(\delta\gamma)F_{\text{cold+i-th,tot}}(V,T)|_{\gamma_T} = 0$ and $\delta\gamma_T = \gamma_T - \gamma_0$ results in

$$\delta\gamma_T = \frac{-\frac{\partial}{\partial\gamma}F_{\text{cold+i-th,tot}}(V,T)\Big|_{\gamma_0}}{\frac{\partial^2}{\partial\gamma^2}F_{\text{cold+i-th,QH}}(V,T)\Big|_{\gamma_0}}, \tag{13}$$

which gives the correction to the axial ratio caused by temperature effects. Expressing free energy as a function of its natural independent state variable [56], i.e., $(\partial/\partial\gamma)F(V,T) = (2V/3\gamma)\sigma^{\mathrm{aniso}}$, Eq. (13) can be rewritten as

$$\delta\gamma_T = \frac{-\left(\frac{2V}{3\gamma_T}\right)\left\langle\sigma^{\mathrm{aniso}}_{\text{i-th,tot}}(V,T)\right\rangle}{\frac{\partial^2}{\partial\gamma^2}F_{\text{cold+i-th,QH}}(V,T)\Big|_{\gamma_0}}. \tag{14}$$

Here, $\sigma^{\mathrm{aniso}} = \sigma_{33}$–$(1/2)(\sigma_{11} + \sigma_{22})$ is the deviatoric stress, where σ_{11}, σ_{22}, and σ_{33} are the uniaxial normal stresses. These can be obtained from QMD alone, without phonon calculations, since zero-point motion does not contribute to system stress. Rearranging the stress tensor for the anharmonic component,

$$\begin{aligned}&\left\langle\sigma^{\mathrm{aniso}}_{\text{i-th,AH}}(V,T)\right\rangle \\ &= \left\langle\sigma^{\mathrm{aniso}}_{\text{i-th,tot}}(V,T)\right\rangle - \sigma^{\mathrm{aniso}}_{\text{cold+i-th,QH}}(V,T) \\ &= \left\langle\sigma^{\mathrm{aniso}}_{\text{i-th,tot}}(V,T)\right\rangle - \left(\frac{3\gamma_T}{2V}\right)\frac{\partial}{\partial\gamma}F_{\text{cold+i-th,QH}}(V,T)\Big|_{\gamma_{\mathrm{T}}},\end{aligned} \tag{15}$$

$F_{\text{i-th,AH}}(V, T; T_{\mathrm{e}} \to 0, \gamma_0 \to \gamma_T)$ can be rewritten as

$$\begin{aligned}&F_{\text{i-th,AH}}(V, T; T_{\mathrm{e}} \to 0, \gamma_0 \to \gamma_T) \\ &= -\left(\frac{2V}{3\gamma_T}\right)^2 \frac{\left\langle\sigma^{\mathrm{aniso}}_{\text{i-th,tot}}(T)\right\rangle\left\langle\sigma^{\mathrm{aniso}}_{\text{i-th,AH}}(T)\right\rangle}{\frac{\partial^2}{\partial\gamma^2}F_{\text{cold+i-th,QH}}(T)\Big|_{\gamma_0}}.\end{aligned} \tag{16}$$

The finite-temperature electronic contribution to the Helmholtz free energy originating from electronic thermal excitation ($F_{\text{e-th}}$) was calculated from single-point DFT calculations with Fermi-Dirac smearing corresponding to $T_{\mathrm{e}}(= T_{\mathrm{i}})$. The cumulative Gibbs free energy was obtained by adding up the computed individual components of a canonical decomposition, i.e.,

$$\begin{aligned}G(V,T) = G_{\mathrm{cold}}(V) + F_{\mathrm{i,QH}}(V,T) + F_{\text{i-th,AH}}(V,T) \\ + F_{\text{e-th}}(V,T) + P_{\mathrm{th}}V,\end{aligned} \tag{17}$$

where the thermal pressure $P_{\mathrm{th}} = P(V,T)$–$P(V,0)$. The thermodynamically most stable structure at each (V,T) point could thereafter be identified by fitting the directly calculated $G(V,T)$ points with an EOS model and identifying the structure with the minimum $G(V,T)$. This has been shown in Fig. 1(c), which gives a graphical overview of the different components of the Gibbs free energy, where G_{cold} is equivalent to $G_{\mathrm{analytic}}(\Gamma; V, \gamma)$ in Fig. 1(b).

For the purpose of setting a reference, Θ is calculated for a quasiharmonic Debye model with the assumption of an isotropic solid with Poisson's ratio σ_P (assumed to have a limiting value of 0.5 in this work),

$$\Theta = \frac{\hbar}{k_{\mathrm{B}}}\sqrt[3]{6\pi^2 V^{1/2} n}\, f(\sigma_{\mathrm{P}})\sqrt{\frac{B_{\mathrm{s}}}{M_{\mathrm{a}}}}, \tag{18}$$

where M_{a} is the atomic mass and B_{s} is the adiabatic bulk modulus, approximated as $B_{\mathrm{s}} \approx \mathrm{B}_{\mathrm{static}}(V, \gamma, T) = V(d^2/du^2)E(V, \gamma, T)$ and

$$f(\sigma_{\mathrm{P}}) = \left\{3\left[2\left(\frac{2}{3}\frac{1+\sigma_{\mathrm{P}}}{1-2\sigma_{\mathrm{P}}}\right)^{3/2} + \left(\frac{1}{3}\frac{1+\sigma_{\mathrm{P}}}{1-\sigma_{\mathrm{P}}}\right)^{3/2}\right]^{-1}\right\}^{1/3}.$$

D. Vibrational transitional spectra

This subsection details the methodology used to calculate the two types of spectra that involve ionic vibrational transitions—inelastic scattering or Raman spectra, and infrared (IR) absorption spectra. The calculations of the vibrational transition spectra require the calculation of the second- and third-order interatomic force constants for the crystal structures, with the first being used to calculate the normal modes of the phonon vibrations, whereas the second is used to calculate the width of the spectra. For this purpose, we resorted to using PHONOPY and PHONO3PY [57], respectively. All such calculations are performed at the Γ point of the 1BZ.

The IR activity is calculated using the Born effective charge tensor $\mathbf{Z}^*$, whose components are

$$Z^*_{xy,\kappa} = \frac{1}{|e|}\frac{\partial\mu_{xy}}{\partial r_{y,\kappa}} = \frac{V}{|e|}\frac{\partial P_x}{\partial r_{y,\kappa}} = -\frac{1}{|e|}\frac{\partial F_{y,\kappa}}{\partial\varepsilon_x} = \frac{1}{|e|}\frac{\partial^2 E}{\partial\varepsilon_x\partial r_{y,\kappa}}, \tag{19}$$

where V is the volume of the unit cell; P is the macroscopic polarization tensor; μ is the electric dipole moment; F is the Hellmann-Feynman force; ε is the electric field; E is the total energy; and x, y denote Cartesian coordinates, with the derivatives being taken at fixed strain and fixed electric field. This can be computed using DFPT calculations. Within the dipole approximation, the IR intensity of an eigenmode can be written as

$$\begin{aligned} I_{\mathrm{IR}}(\mathbf{\Gamma}:\lambda) &\propto \sum_{x=1}^{3}\left|\sum_{\kappa=1}^{N_{\mathrm{a}}}\sum_{y=1}^{3}\frac{\partial\mu_{xy}}{\partial r_{y,\kappa}}X_{y,\kappa}(\lambda)\right|^2 \\ &= \sum_{x=1}^{3}\left|\sum_{\kappa=1}^{N_{\mathrm{a}}}\sum_{y=1}^{3}Z^{*}_{xy,\kappa}X_{y,\kappa}(\lambda)\right|^2, \end{aligned} \tag{20}$$

where $X_{\mathrm{y},\kappa}(\lambda)$ is the normalized eigendisplacement along the direction y of atom κ, $\mathbf{X}_{\kappa}(\lambda) = \mathbf{W}_{\kappa}(\lambda)/\sqrt{m_{\kappa}}$, $\mathbf{W}_{\kappa}(\lambda)$ represents the eigenvector defined in Eq. (5), and λ represents the phonon band index. The outermost summation stems from the fact that IR intensities are the sum of the uniaxial intensities.

To calculate the Raman activity, Placzek's expression [58] for nonresonant Raman intensity for an eigenmode in the Stokes process,

$$I_{\mathrm{Raman},xy}(\mathbf{\Gamma}:\lambda) \propto \left|\mathbf{e}_{\mathrm{I}}\cdot\sum_{\kappa=1}^{N_{\mathrm{a}}}\frac{\partial\boldsymbol{\alpha}}{\partial\mathbf{r}_{\kappa}}\boldsymbol{X}_{\kappa}(\lambda)\cdot\mathbf{e}_{\mathrm{S}}\right|^2\frac{n_{\mathrm{BE}}(\lambda,T)+1}{\nu_{\lambda}}, \tag{21}$$

was used, where $\boldsymbol{\alpha}$ is the microscopic polarizability tensor; $\mathbf{e}_{\mathrm{I}}$ and $\mathbf{e}_{\mathrm{S}}$ are unit vectors along the direction of incidence and scattering, respectively; n_{BE} is the Bose-Einstein distribution function,

$$n_{\mathrm{BE}}(\lambda,T) = \left[\exp\left(\frac{h\nu_{\lambda}}{k_{\mathrm{B}}T}\right)-1\right]^{-1}, \tag{22}$$

and ν_{λ} is the frequency of band index λ. Since the long-wavelength limit ($\mathbf{k}\to 0$) of the macroscopic dielectric tensor determines optical properties of a system, the high-frequency macroscopic dielectric constant $\in^{\infty}$ is the variable of interest here. Now, $\boldsymbol{\alpha}$ is related to $\in^{\infty}$ as

$$\begin{aligned} \frac{\partial\alpha_{xy}}{\partial r_{y,\kappa}} &= \frac{1}{N_{\mathrm{a}}}\frac{\partial\chi_{xy}}{\partial r_{y,\kappa}} = \frac{1}{N_{\mathrm{a}}}\frac{\partial^2 P_x}{\partial r_{y,\kappa}\partial\varepsilon_y} \\ &= -\frac{1}{N_{\mathrm{a}}V}\frac{\partial^2 F_{y,\kappa}}{\partial\varepsilon_x\partial\varepsilon_y} \equiv \frac{1}{N_{\mathrm{a}}}\frac{\partial\in^{\infty}_{xy}}{\partial r_{y,\kappa}}, \end{aligned} \tag{23}$$

since the susceptibility $\chi = \in -1$ and $\chi = N_{\mathrm{a}}\alpha$, by virtue of the local and ambient fields being equal. This leads to

$$I_{\mathrm{Raman},xy}(\mathbf{\Gamma}:\lambda) \propto \left|\sum_{\kappa=1}^{N_{\mathrm{a}}}\frac{\partial\in^{\infty}_{xy}}{\partial r_{\kappa}}X_{y,\kappa}(\lambda)\right|^2\frac{n_{\mathrm{BE}}(\lambda,T)+1}{\nu_{\lambda}} \tag{24}$$

along a plane in which spatial axes x and y lie. The cumulative Raman intensity is obtained by using [59]

$$\begin{aligned} I_{\mathrm{Raman}}(\mathbf{\Gamma}:\lambda) &= 5(I_{11}+I_{22}+I_{33})^2 + \tfrac{7}{2}(I_{11}-I_{22})^2 \\ &\quad + \tfrac{7}{2}(I_{11}-I_{33})^2 + 21\left(I_{12}^2+I_{13}^2+I_{23}^2\right), \end{aligned} \tag{25}$$

with indices 1, 2, and 3 referring to the three spatial directions.

It should be noted that each band index λ corresponds to a different phonon normal mode of atomic vibration; whether that particular mode is Raman active or IR active or both is determined from its space group (see Table VII in Sec. III) by the selection rules.

The aforementioned analysis yields the intensities of the vibration spectra, but in order to capture the temperature effect, the full width at half maximum (FWHM) of the peaks must be computed as well. Since optical phonon lifetimes are predominantly determined from three-phonon interactions, we evaluated the phonon lifetime $\tau_{\lambda}(\Gamma:\omega_{\lambda},T)$ from the third-order interatomic force constants [57]:

$$\begin{aligned} \frac{1}{\tau_{\lambda}(\mathbf{\Gamma}:\omega_{\lambda},T)} &\equiv 2\Lambda_{\lambda}(\mathbf{\Gamma}:\omega_{\lambda},T) \\ &= \frac{36\pi}{\hbar^2}\sum_{\lambda_1\lambda_2}\sum_{x,y,z}\left|\Phi^{(3)}_{xyz}\right|^2\{[1+n_{\mathrm{BE}}(\lambda_1,T)+n_{\mathrm{BE}}(\lambda_2,T)] \\ &\quad\times\delta\left(\omega_{\lambda}-\omega_{\lambda_1}-\omega_{\lambda_2}\right)+[n_{\mathrm{BE}}(\lambda_1,T)-n_{\mathrm{BE}}(\lambda_2,T)] \\ &\quad\times\left[\delta\left(\omega_{\lambda}+\omega_{\lambda_1}-\omega_{\lambda_2}\right)-\delta\left(\omega_{\lambda}-\omega_{\lambda_1}+\omega_{\lambda_2}\right)\right]\}, \end{aligned} \tag{26}$$

where Λ_{λ} refers to the linewidth of the phonon eigenmode λ and $\Phi^{(3)}_{xyz}$ is the third-order interatomic force constant from Eq. (3). This quantity can be used to estimate the width of the Raman/IR peaks, when fitted in a Lorentzian,

$$I(\mathbf{\Gamma}:T) = \sum_{\lambda}I(\mathbf{\Gamma}:\lambda)\frac{1}{\pi}\frac{\frac{1}{2}\Lambda_{\lambda}(\mathbf{\Gamma}:T)}{(\nu-\nu_{\lambda})^2+\left[\frac{1}{2}\Lambda_{\lambda}(\mathbf{\Gamma}:T)\right]^2}, \tag{27}$$

corresponding to a temperature T.

However, the above expression separately takes only two effects into account: the location of the normal modes at $T = 0$ K and superimposition of the finite-temperature spread $\Lambda_{\lambda}(\mathbf{\Gamma}:T)$. To gauge the finite-temperature effects, i.e., (1) the shift in normal modes caused by crystal thermal expansion

$$\Delta\nu[V(T)] \approx \nu_{\mathrm{phonon}}[V(T)] - \nu_{\mathrm{phonon}}(T=0), \tag{28}$$

TABLE I. Pressure-temperature combinations for which UPSEX runs were performed.

Temperature (K)	Pressure (GPa)
0	5, 10, 12, 14, 16, 18, 20, 25, 30, 40, 50, 75, 100, 200, 300, 500, 1000, 2000, 2300, 2500, 2700, 2800, 3000, 3500, 3700, 3800, 3900
300	14, 16, 18, 34, 36, 38
500	38, 40

TABLE II. Classification details of the different crystal structures.

		Space group		Point group	
Crystal structure	Pearson symbol	Short	Number	Hermann-Mauguin notation	Schönflies notation
Cubic diamond (cd)	$cF8$	$Fd\bar{3}m$	227	$m\bar{3}m$	O_h
Body-centered Tetragonal (bct/β-Sn)	$tI4$	$I4_1/amd$	141	$4/mmm$	D_{4h}
Body-centered Orthorhombic	$oI4$	$Imma$	64	mmm	D_{2h}
Simple hexagonal (sh)	$hP1$	$P6/mmm$	191	$6/mmm$	D_{6h}
Hexagonal close-packed (hcp)	$hP2$	$P6_3/mmc$	194	$6/mmm$	D_{6h}
Double hexagonal Close-packed (dhcp)	$hP4$	$P6_3/mmc$	194	$6/mmm$	D_{6h}
Base-centered Orthorhombic	$oC16$	$Cmce$	74	mmm	D_{2h}
Face-centered cubic (fcc)	$cF4$	$Fm\bar{3}m$	225	$m\bar{3}m$	O_h
Body-centered cubic (bcc)	$cI2$	$Im\bar{3}m$	229	$m\bar{3}m$	O_h
Simple cubic (sc)	$cP1$	$Pm\bar{3}m$	221	$m\bar{3}m$	O_h

and (2) the change in the intensity peaks,

$$\Delta I_{\text{peak}}(\boldsymbol{\Gamma} : T) \propto \Delta G_{\max}(\boldsymbol{\Gamma} : \omega), \tag{29}$$

we take the aid of the power spectrum constructed from phonon eigenvector-projected atomic velocities. This was achieved by using DYNAPHOPY [60], which calculates the full power spectra,

$$G(\mathbf{k} : \omega) = 2 \sum_{\kappa,x} \int_{-\infty}^{\infty} \langle v_{\kappa,x}^{\mathbf{k}*}(0) v_{\kappa,x}^{\mathbf{k}}(t) \rangle e^{i\omega t}\, dt, \tag{30}$$

and the phonon frequencies $\nu_{\text{phonon}}[V(T)]$ were obtained by using atomic velocities v from QMD simulations. With these two finite-temperature corrections, the temperature-dependent Raman and IR spectra can be calculated.

III. RESULTS AND DISCUSSIONS

The section contains all of the results, culminating in the complete pressure-temperature (P-T) phase diagram of silicon. Section III A concerns the cold-curve structure searches; Sec. III B describes all of the free-energy calculations, including the quasiharmonic and anharmonic components to capture finite-temperature effects; Sec. III C is focused solely on determining the melt curve; Sec. III D presents the holistic phase diagram with additional observations on electronic properties along the cold curve; and, finally, Sec. III E details all of the Raman and IR spectra calculations.

A. Structure search using evolutionary algorithms

The evolutionary algorithm USPEX [61–63] was used to predict the most stable structures for a given pressure. The structure relaxations were performed using the DFT code Vienna *ab initio* simulation package (VASP) [64–66], which uses the Perdew-Burke-Ernzerhof (PBE) formulation [67] of the generalized gradient approximation (GGA) [68] exchange-correlation functional and employs projector augmented wave (PAW) pseudopotentials [69]. For the Si atoms, PAW pseudopotentials with an 0.85-Å cutoff radius were used with the $2s^2\,2p^6\,3s^2\,3p^2$ electrons being treated as valence electrons. The plane-wave kinetic energy cutoff was 1100 eV,

TABLE III. Optimal k mesh for equilibrium geometries of the structures.

Crystal Structure	Pressure (GPa)	k mesh
cd	11	21 × 21 × 21
bct/β-Sn	13	15 × 15 × 23
Imma	15	15 × 21 × 23
sh	29	21 × 21 × 15
hcp	48	21 × 21 × 17
Cmce	41	21 × 23 × 15
dhcp	52	21 × 21 × 17
fcc	168	23 × 23 × 23
bcc	3115	29 × 29 × 29
sc	3839	31 × 31 × 31

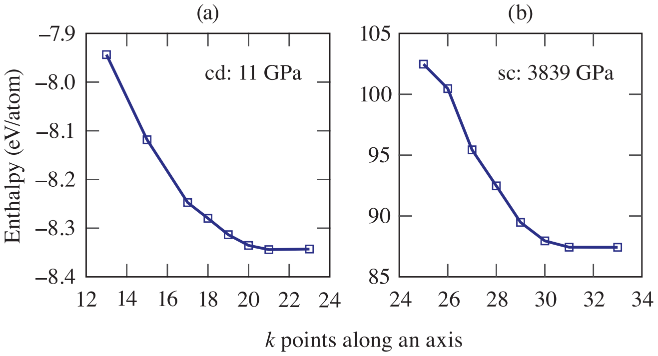

FIG. 2. Convergence of enthalpy per atom for (a) low-pressure and (b) high-pressure cases against a number of uniaxial k points.

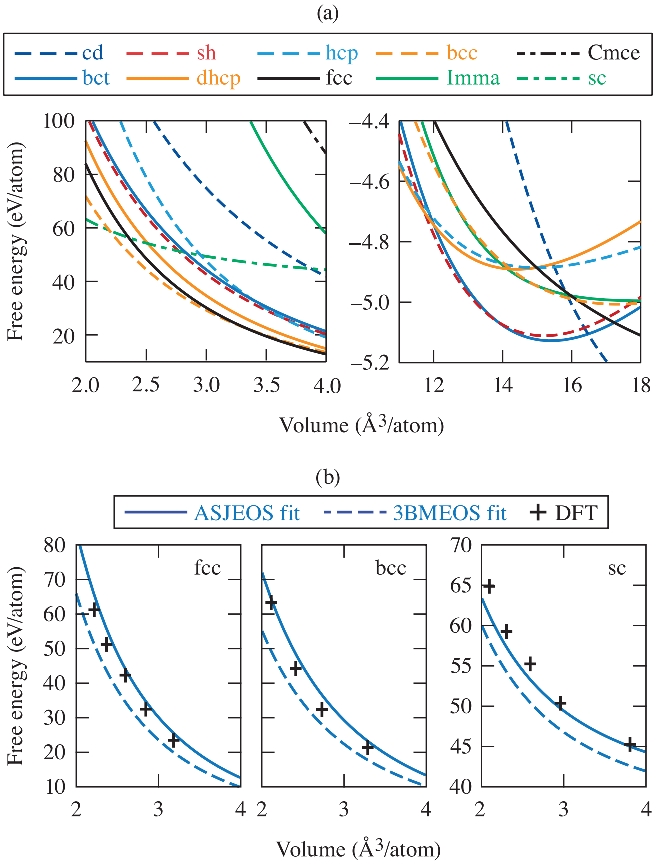

FIG. 3. (a) Helmholtz free-energy–pressure (F-P) fits along the cold compression curve for the low-pressure (left) and the high-pressure (right) domains. (b) The comparison of fitting errors between the ASJEOS and 3BMEOS relative to discrete data.

and the Brillouin zone was sampled with a resolution of $2\pi \times 0.04\,\text{Å}^{-1}$. For the structure search, the first generation of 10 to 40 structures was created randomly. All structures were relaxed at 0 K and at a constant pressure after being run over 20–40 subsequent generations until minimization and convergence of the fitness criteria (enthalpy). The structures having the lowest enthalpy were used as the seed for creating offspring of the next generation. Each subsequent generation was created using 60% of the best structures of the previous generation using a combination of heredity (65%), randomness (10%), soft mutation (10%), and lattice mutation (15%). This procedure was repeated for 16 different cases with $N_a = 1, 2, 3, \ldots, 16$ atoms, respectively, in a unit cell under periodic boundary conditions, with three to five repetitions of the searches being performed for each target pressure and N_a. The structure searches yielded eight stable structures: cubic diamond (cd), body-centered tetragonal/beta-tin (bct/β-Sn), simple hexagonal (sh), hexagonal close-packed (hcp), face-centered cubic (fcc), body-centered cubic (bcc), and simple cubic (sc), and a metastable double hexagonal close-packed (dhcp) structure along with hcp.

Using *a priori* knowledge from earlier experiments, we also considered two other structures: body-centered orthorhombic (*Imma*) and base-centered orthorhombic (*Cmce*). The *Imma* structure was observed in the pressure range of 13–16 GPa [35], whereas the *Cmce* structure was indicated in an x-ray diffraction experiment at pressures of ~40 GPa [36]. To computationally find these two structures, a few USPEX evolutionary metadynamics [70] runs were also performed at 300 and 500 K, starting with β-Sn, sh, and hcp to obtain the targeted structures of *Imma*, *Cmce*, and *dhcp*, respectively, but instead they yielded β-Sn, dhcp, and dhcp, respectively. The necessity of a rather similar starting structure renders this method impractical for these particular cases. The pressure-temperature combinations for which USPEX runs were performed are shown in Table I, and the crystallographic classification information for all of the forenamed ten structures has been tabulated in Table II.

B. Solid-state thermodynamic calculations

The lattice constants obtained at particular state (P, $T = 0\,\text{K}$) points using a structure search were used as starting points to scan the entire pressure domain up to ~4 TPa along the cold compression ($T = 0\,\text{K}$) curve. The upper bound of the pressure was imposed by the limitation of the 12-active-electron PAW potential we used for our computations. In addition, it is to be noted that the orthorhombic structures have internal parameters (x, y, z) that must be separately optimized. To minimize computational time, however, such internal parameter optimization was performed only after optimizing the lattice constants and axial ratios, at particular pressures: for *Imma* at 6.2, 10.7, and 17.9 GPa, and for *Cmca* at 2.8, 10.9, 22.4, 35.1, and 47.9 GPa.

TABLE IV. ASJEOS fitting parameters for Gibbs free energy at $T = 0\,\text{K}$.

Crystal Structure	a	b	c	d	α	β	γ
cd	7.8025	2.3478	5.4701	9.2939	6.4432	2.0774	3.1110
bct/β-Sn	3.8974	3.5316	2.9632	7.7571	3.7861	3.0125	9.2338
Imma	2.4169	8.2119	7.4469	4.8679	8.1158	4.7092	4.3021
sh	4.0391	0.1540	1.8896	4.3586	5.3283	2.3049	1.8482
hcp	0.9645	0.4302	6.8678	4.4678	3.5073	8.4431	9.0488
Cmce	1.3197	1.6899	1.8351	3.0635	9.3900	1.9476	9.7975
dhcp	9.4205	6.4912	3.6848	5.0851	8.7594	2.2592	4.3887
fcc	9.5613	7.3172	6.2562	5.1077	5.5016	1.7071	1.1112
bcc	5.7521	6.4775	7.8023	8.1763	6.2248	2.2766	2.5806
sc	0.5978	4.5092	0.8113	7.9483	5.8704	4.3570	4.0872

TABLE V. Equilibrium lattice parameters for the crystal structures.

Crystal structure	*a* (Å)	*b*/*a*	*c*/*a*
cd	5.457		
bct/β-Sn	4.762		0.548
Imma	4.735	0.948	0.540
sh	2.542		0.942
hcp	2.526		1.611
Cmce	8.019	0.598	0.596
dhcp	2.744		3.250
fcc	3.408		
bcc	2.682		
sc	2.463		

The convergence tests for the Monkhorst-Pack [71] k points were performed for each of the structures by checking the enthalpy per atom in the single-point calculations. Due to the large span of pressures scanned, we report in Table III only the k mesh chosen near the equilibrium geometries (discussed later in this subsection) for each of the structures. For higher pressures than those at which the equilibrium geometries exist, we increased the size of the k mesh to take into account the increased size in the reciprocal space. The results for the convergence tests for two specific structures are shown in Fig. 2, where the convergence criterion was selected to be 0.5 meV/atom. They show that the chosen k points listed in Table III give convergent results.

The discrete cold-compression-curve Gibbs free-energy (G) data (i.e., enthalpy) obtained from single-point calculations for each of the structures were fitted with ASJEOS [Eq. (2)] [49] and third-order Birch-Murnaghan EOS (3BMEOS) [72], shown in Fig. 3. It was observed from Fig. 3(b) that far away from equilibrium, at pressures exceeding ~2 TPa, the discrepancy between the fit values and the computed discrete data points at a particular pressure was much lower for ASJEOS than for 3BMEOS. As such, we eventually used the ASJEOS fit across the entire pressure domain. The fitting parameters have been tabulated in Table IV and the equilibrium geometries in Table V. The fits for all the structures are shown in Fig. 3(a), whereas ASJEOS and 3BMEOS are compared in Fig. 3(b). It should be noted that the fits progressively become less accurate when moving this far away from the equilibrium. We determine the thermodynamically most stable structure of silicon by choosing the one with the lowest Gibbs free energy at a given pressure.

To examine the mechanical stability of each structure, we calculated their PDOS (discussed in the next section in detail) along the cold curve. These required DFPT calculations, which were performed in 128-atom supercells with the convergence criteria being the electronic energy error $<10^{-8}$ eV/atom and the ionic force error $<10^{-3}$ eV/Å. The PDOS was analyzed for multiple geometries of each structure, and the results for the TPa-range geometries are shown in Fig. 4. The absence of imaginary phonon frequencies indicates the structures are dynamically stable.

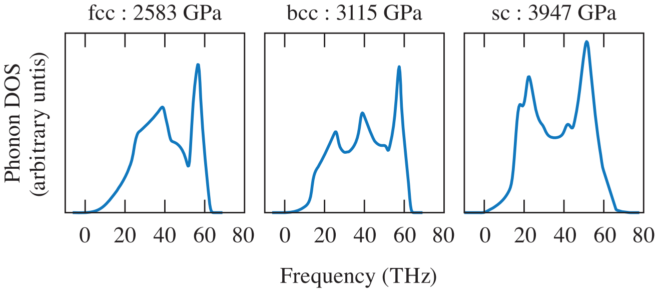

FIG. 4. Phonon density of states (DOS) for the fcc, bcc, and sc structures at TPa pressures showing dynamical stability.

An apt gauge of the applicability of the QH analysis for the structure in question is to check for the effect of finite electronic temperature T_e, despite having ions at 0 K. This is shown in Fig. 5, which illustrates the limitations of QH analysis in cases of orthorhombic geometries, such as *Cmce* and *Imma*. At the bare minimum, QH analysis should be insensitive to electronic temperatures, which is not the case for these two structures. For more-ordered structures, such as the cubic ones, the QH approximation seems to hold for temperatures below the melt curve (discussed in Sec. III C). The same observation holds true for the hexagonal structures, even though their PDOS is not shown in Fig. 5.

The effect of anharmonicity on the Helmholtz free energy was evaluated after completing the melt-curve calculations to ensure that the reference temperature (T_{ref}) selected was such that $T_{\text{melt}} > T_{\text{ref}} > \Theta$. Figure 6 summarizes the choices of our reference temperature along different isochores, which

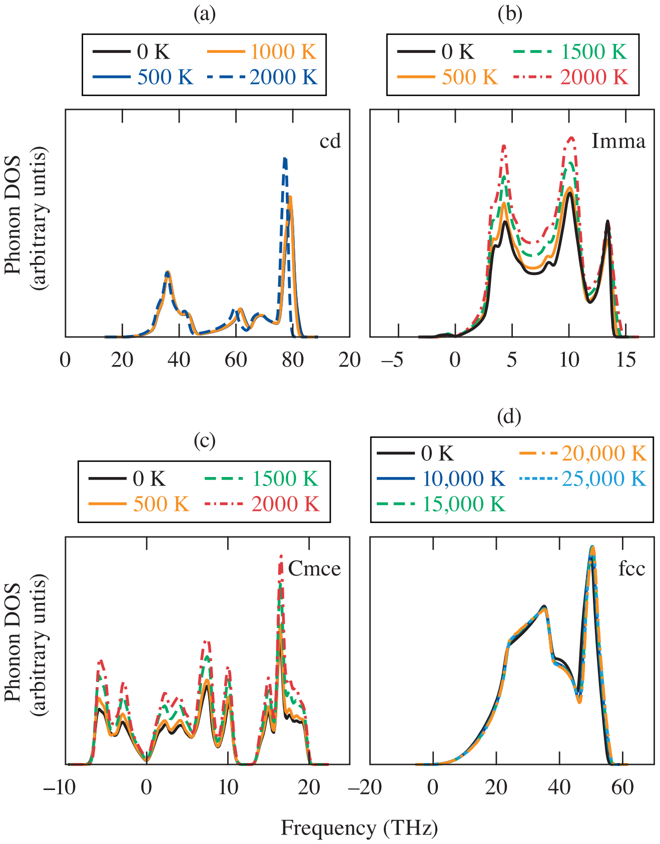

FIG. 5. PDOS at relevant electronic temperatures T_e as indicated in the legends, while maintaining ionic temperature $T_i = 0$.

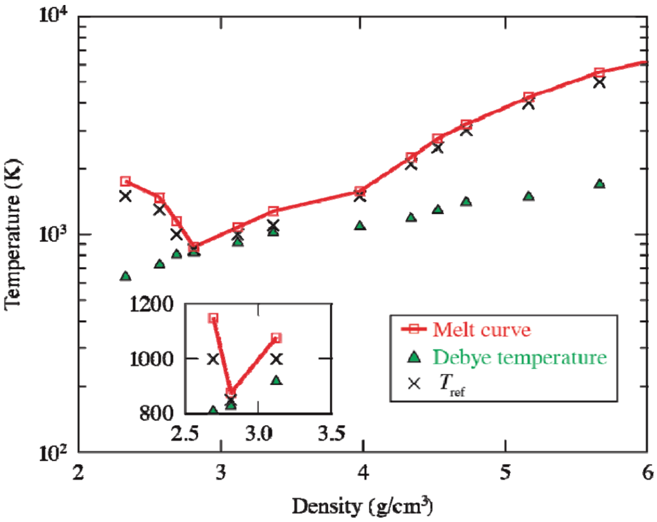

FIG. 6. Values of melting point, reference temperature for anharmonicity calculations, and Debye temperature for different isochores. The inset shows the zoomed view of the figure near the slope inversion.

were always higher than the Debye temperature of the corresponding solid-state structure. The anharmonic contribution $F_{\text{i-th,AH}}$ was found to be of the same order of magnitude as the harmonic contribution, especially for the cd, *Imma*, and *Cmce* structures. We tested finite-size effects by carrying out QMD simulations with a maximum 1024 atoms in the supercell, which gave <0.6% change in the free-energy results.

Delving into the different components of the Helmholtz free energy at $T = 500$ K, as listed in Table VI, shows that the anharmonic contributions are negligible for the fcc, bcc, and sc structures, in clear contrast to the cd, *Imma*, *Cmce*, and dhcp structures, where the anharmonic contribution $F_{\text{i-th,AH}}(V, T)^{(1)}$ [see Eq. (10)] is of the same order as the harmonic one. Also, the component $F_{\text{i-th,AH}}(V, T)^{(2)}$, corresponding to the change in axial ratios with temperature, clearly has a negligible contribution to the total anharmonic free energy.

Computing the cumulative Gibbs free energy $G(V,T)$ along each isotherm allows one to determine the most stable solid-state structures at finite temperatures. This forms the basis of the solid-state pressure-temperature (P-T) phase diagram. Figure 7 shows the computed results from an isothermal point of view, i.e., the density-pressure (ρ-P) EOS for $T = 100$ K, which demonstrates the jump in density due to phase transitions as is characteristic of first-order phase transitions. Quantitatively, this corresponds to an approximately tenfold increase in density on compressing from ambient pressure to 4 TPa.

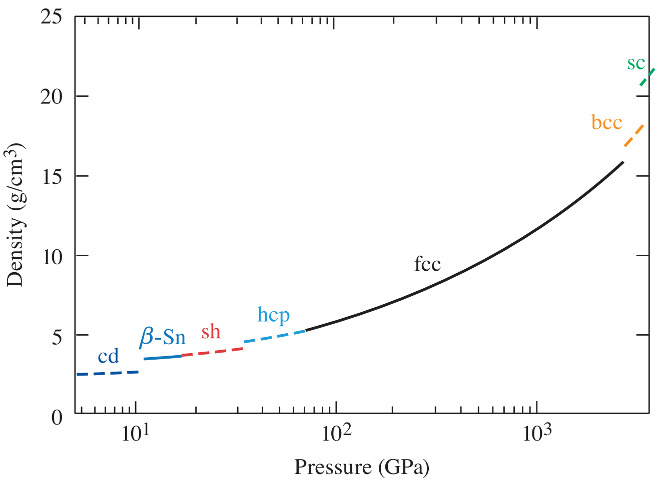

FIG. 7. Density-pressure (ρ-P) plot showing discontinuities in ρ at pressures corresponding to phase transitions at $T = 100$ K.

C. Solid-liquid phase transitions

Quantum molecular dynamics simulations, within the Born-Oppenheimer approximation, were performed using a canonical (constant-*NVT*) ensemble to determine the melting points $T_{\rm melt}$, while incrementally increasing system temperature along isochores. This "heat until melts" method [73,74] is an established approach that suffers from the drawback of overpredicting $T_{\rm melt}$. This is mostly because perfect crystals in simulations undergo phase transitions in bulk, whereas anisotropic defect-laden imperfect crystals in experiments start localized transitions near defects, which hastens the entire solid-liquid phase change. VASP was used for the QMD calculations, with the temperature being controlled via a Nosé-Hoover thermostat [75]. Instead of using Monkhorst-Pack k mesh, we resorted to the use of a single special k point (1/4, 1/4, 1/4) for sampling the Brillouin zone (1BZ), as was introduced by Baldereschi [76]. Supercells were used, with 216–256 atoms, with the ionic time step ranging from 0.26 to 0.63 fs for a total of 4000–6500 QMD ionic steps. Time steps were selected after being considered to be an inverse

TABLE VI. The different contributions (in eV/atom) to the free energy at 500 K.

Structure	Pressure (GPa)	$F_{e\text{-th}}$ (eV/atom)	$F_{\rm i,QH}$ (eV/atom)	$F^{(1)}_{\text{i-th,AH}}$ (eV/atom)	$F^{(2)}_{\text{i-th,AH}}$ (eV/atom)
cd	11	–4.1721	0.4176	0.1344	
Imma	15	–3.7807	0.4687	0.1821	0.0047
Cmce	41	–1.4281	0.1879	0.0863	0.0072
dhcp	52	–1.1071	0.1514	0.0605	0.0021
fcc	2583	76.4725	1.2636	0.0022	
bcc	3115	87.8349	1.5747	0.0104	
sc	3839	101.4307	1.8380	0.0398	

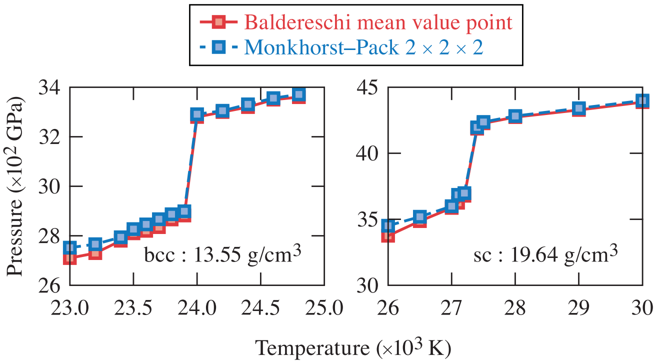

FIG. 8. Convergence of pressure with respect to different reciprocal-space (k-space) discretization schemes chosen during *NVT*-QMD simulations.

function of the square root of temperature and the cube root of the density. The combination of ionic step size and total number of steps was selected for each QMD simulation such that the total physical time for the system was always more than 2 ps.

Convergence tests for the k mesh are illustrated in Fig. 8, which clearly demonstrates that the Baldereschi mean-value point is as accurate as a $2 \times 2 \times 2$ Monkhorst-Pack k mesh near the phase-transition boundary, while deviations occur as we move away from the melt curve in the solid regime. The two panels in the figure correspond to two isochores, one for bcc at $13.55\,\mathrm{g/cm^3}$ and the other for sc at $19.64\,\mathrm{g/cm^3}$, which both yield the same conclusion as discussed here.

To detect melting in an *NVT*-QMD simulation, we used a combination of checking the ion-ion radial pair correlation function,

$$g(r) = \frac{V}{4\pi r^2 N_{\mathrm{a}}^2}\left\langle \sum_i \sum_{j\neq i} \delta(r - r_{ij}) \right\rangle, \tag{31}$$

and tracking for abrupt changes in Gibbs free energy (G) and pressure (P) with increasing temperatures along an isochore. This is illustrated in Fig. 9, which shows the changes for [(a)–(c)] a low-pressure cd and [(d)–(f)] a high-pressure bcc geometry. The $g(r)$, upon transition from a solid to a liquid state, changes from having multiple discrete peaks to just one prominent peak corresponding to the first coordination sphere. G always exhibits a jump owing to absorption of the latent heat of melting, whereas P can show a jump or a drop. The interpretation of the drop in P for cd and a jump for all other structures [only the case of bcc is shown in Figs. 9(d)–9(f)] is discussed in a later subsection.

We fit our discrete melt-curve predictions T_{melt} with the Kechin equation [77],

$$T_{\mathrm{melt}}(P) = T_0\left(1 + \frac{P_m - P_0}{a_1}\right)^{a_2} e^{-a_3(P_m - P_0)}, \tag{32}$$

in the cd and the other structures separately. This was done to ensure that the opposing isochoric pressure change trends for cd vis-à-vis other structures were accurately

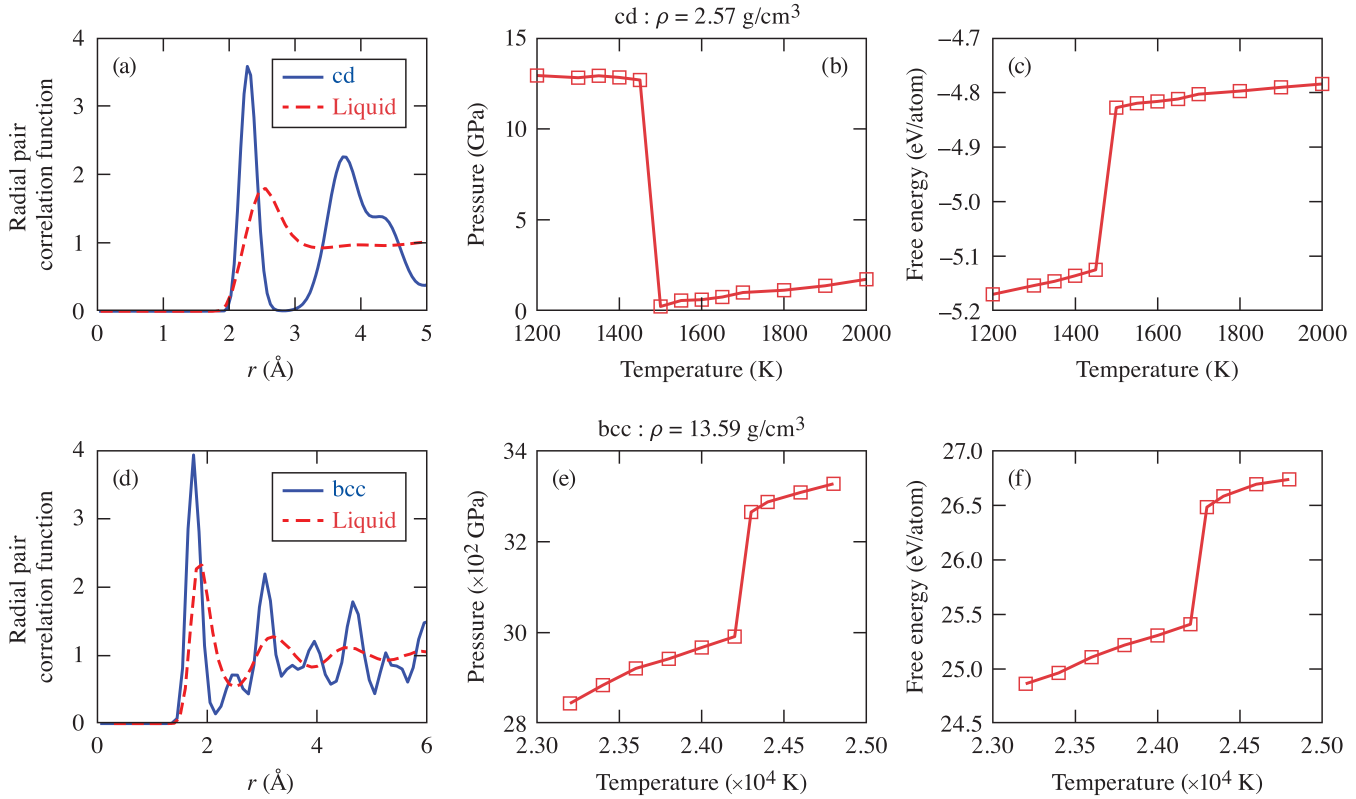

FIG. 9. The change in nature of the radial pair distribution function (left), jump/drop in pressure (center), and jump in free energy (right) used as a signature to detect solid-liquid phase transition, i.e., melting in *NVT*-QMD simulations.

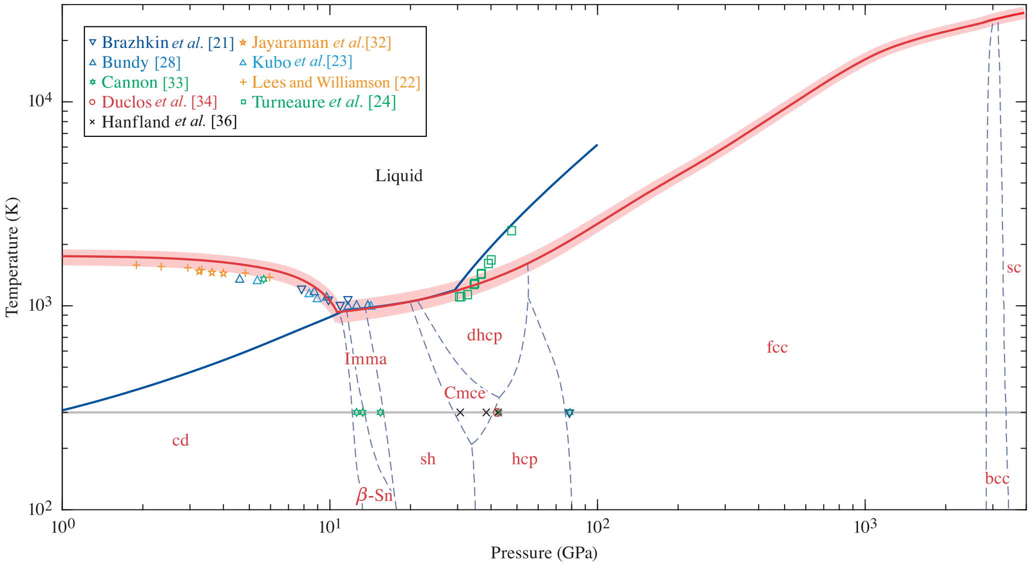

FIG. 10. Pressure-temperature (P-T) phase diagram of silicon predicted using first-principles methodology. Here, the gray horizontal line represents the $T = 300$ K isotherm, whereas the solid blue line represents the principal shock Hugoniot. The discrete data points, which are also labeled in the legend, correspond to experimentally observed phase-transition points [21–24,28,32–34,36].

captured. The values of these constants for the cd branch of the melt curve are $T_0 = 92.37$ K, $P_0 = 21.31$ GPa, $a_1 = 2.27$ GPa, $a_2 = 1.983$, and $a_3 = 0.013$, whereas the values for the remainder of the melt curve are $T_0 = 10\,458.3$ K, $P_0 = 1114.48$ GPa, $a_1 = 783.56$ GPa, $a_2 = 4.565$, and $a_3 = 3.755$.

D. Phase diagram and important observations

The overall P-T phase diagram, spanning up to $P = 4$ TPa and $T = 26\,000$ K, is shown in Fig. 10 with experimental melting points and solid-solid phase transitions marked as shown in the legend. We can observe good agreement between previous experiments with our melting temperature predictions within ±150 K up to ∼35 GPa. Because of reasons mentioned in Sec. III D (imperfect crystals in experiments), the observed melting temperatures are consistently ∼50–150 K lower than our predictions. Previously observed experimental solid-solid transitions along the $T = 300$ K isotherm also agree well with our calculated transition points in the corresponding pressure ranges. The principal shock Hugoniot (solid blue line in Fig. 10) for a shock wave is determined by solving the Rankine-Hugoniot equation with our multiphase EOS data. Overall, the Hugoniot shows good agreement with the recent experimental data [24,25]. The contrasting slopes of the cd branch of the melt curve and the others can be interpreted using the Clausius-Clapeyron relation,

$$\frac{dP}{dT} = \frac{L}{T_{\text{melt}}\Delta v}, \tag{33}$$

whereby one can see that $dP/dT < 0$ for cd, which would imply that the change in specific volume $\Delta v (\sim 1/\rho)$ is negative; i.e., density increases with increasing temperatures for cd along an isobar (negative thermal expansion coefficient). Another way to interpret this is that a cd isochore in the P-T space would have a negative slope. This critical observation

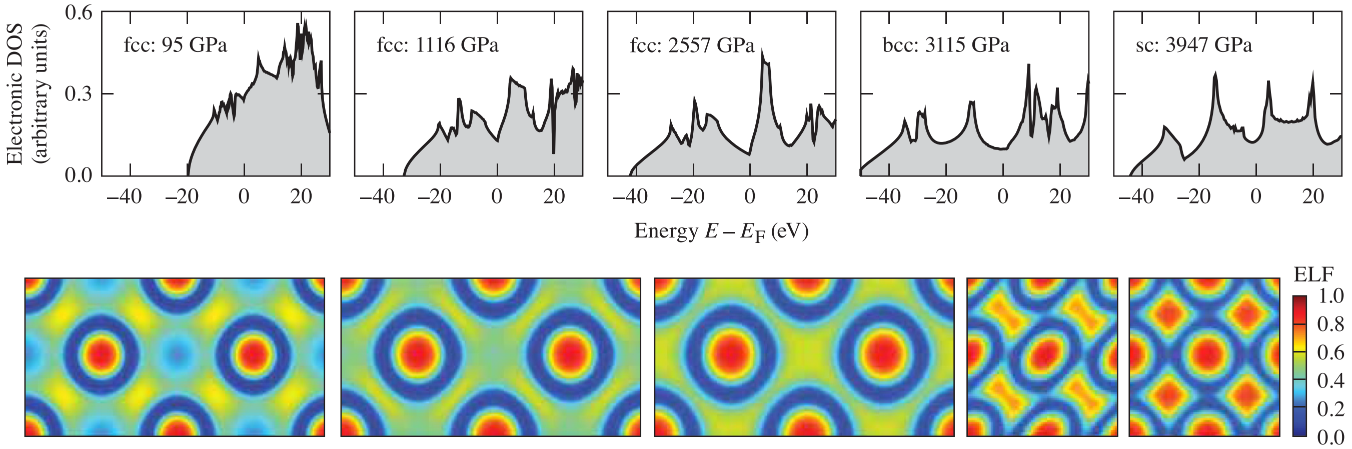

FIG. 11. (Top) Electronic density of states (EDOS) and (bottom) electron localization function (ELF) with increasing pressure for the cubic high-pressure structures. For the EDOS, the Fermi energy (E_F) has been subtracted from the electronic energies.

TABLE VII. Character tables for Raman- and IR-active normal modes of the structures of silicon. The point group notation has been listed in Table II.

Point group	Structures	Raman-active modes	IR-active modes
O_h	cd	T_{2g}	T_{1u}
	fcc	E_g, T_{2g}	T_{1u}
	bcc		T_{1u}
	sc		T_{1u}
D_{2h}	*Imma*	A_g	B_{1u}, B_{2u}
	Cmce	A_g, B_{1g}, B_{2g}, B_{3g}	B_{1u}, B_{2u}, B_{3u}
D_{4h}	β-Sn	B_{1g}, E_g	A_{2u}
D_{6h}	sh	A_{1g}, E_{2g}	A_{2u}
	hcp	E_{2g}	A_{2u}
	dhcp	E_{2g}	E_{1u}, A_{2u}

has an important effect in explaining the observations in the next subsection. The opposite is true for the remainder of the melt curve since dP/dT is positive.

Pressure-induced phase transitions generally follow the *pressure-coordination rule* by Neuhaus [78] (with increasing pressure, an increase of the coordination number takes place) and the *pressure-distance paradox* by Kleber [79] (when the coordination number increases according to the previous rule, the interatomic distances also increase). Here, the fcc-to-bcc-to-sc transition corresponds to a reduction in coordination number from 12 to 8 to 6 and a decrease in minimum interatomic distance. To explain this anomalous fcc-to-bcc-to-sc transition after a pressure span of ~2.8 TPa, where fcc is stable, we looked into the electron distribution. A dip had started to develop in the electronic DOS near the Fermi level, as can be seen in Fig. 11 (top). This dip becomes more pronounced with increasing pressures along the cold curve for fcc but retains more or less the same nature for bcc and sc. Consequently, neither bcc nor sc exhibits electride behavior up to 4 TPa. To further delve into this particular concern, we looked into the electron localization function (ELF) [80]:

$$\begin{aligned}\mathrm{ELF}_\sigma(\mathbf{r}) &= \frac{1}{1+\chi_\sigma^2(\mathbf{r})},\\ \chi_\sigma(\mathbf{r}) &= \frac{D_\sigma(\mathbf{r})}{D_\sigma^0(\mathbf{r})},\\ D_\sigma(\mathbf{r}) &= \sum_{i=1}^{N_\sigma}|\nabla\Psi_i(\mathbf{r})|^2 - \frac{1}{4}\frac{|\boldsymbol{\nabla}\rho_\sigma(\mathbf{r})|^2}{\rho_\sigma(\mathbf{r})},\end{aligned} \tag{34}$$

where $D_\sigma(\mathbf{r})$ is the Pauli kinetic energy density, i.e., the difference between the total fermionic and the bosonic kinetic energy densities; $D_\sigma^0(\mathbf{r})$ is the same for a uniform electron gas; and $\rho_\sigma(\mathbf{r})$ is the electron spin density. The corresponding ELF isosurface plots are shown in Fig. 11 (bottom), which shows that electrons move from the hybridized orbital space to the interstitial space, stabilizing the ionic structure at higher pressures. This is akin to observations in the paired *Cmce* structure in dense lithium [81] and the formation of band-gap electrides in calcium [82].

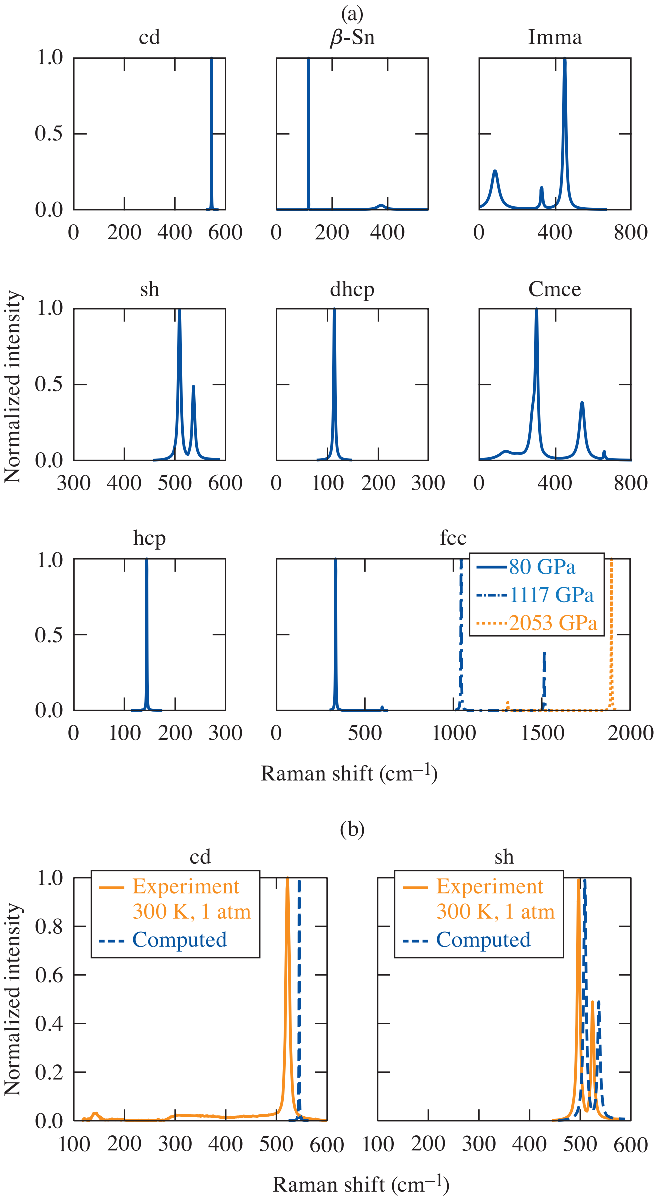

FIG. 12. (a) Raman spectra at 500 K for all the structures of silicon mentioned in this paper; (b) comparison with experimentally available data [83,84].

E. Raman and IR spectra

An analysis, using the phonon spectra, is used to calculate the normal vibrational modes of the different structures yielding the characteristic frequencies. Using point group symmetry character tables, these normal modes can be sorted as to whether they are Raman active, IR active, or neither. This information has been tabulated in Table VII for all the structures of silicon mentioned in this work.

The calculated Raman spectra at 500 K are shown in Fig. 12(a) for all the structures that have Raman-active modes, including three separate cases for fcc to demonstrate the increase in Raman shift with pressure. Figure 12(b) compares computed and experimental data for cd [83] and sh [84], which demonstrate similar peaks. It should be noted, however, that the experimental data for both cd and sh are for

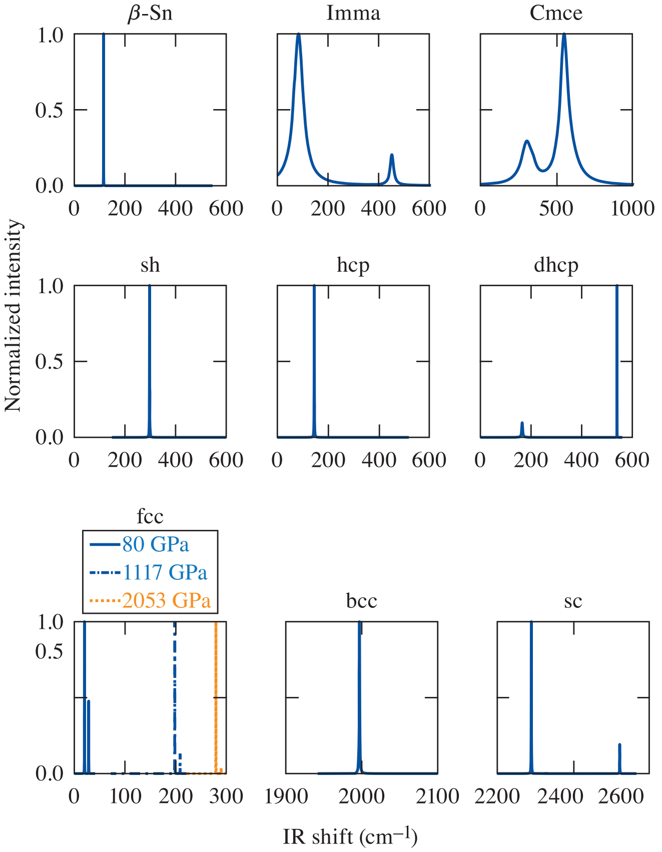

FIG. 13. Infrared spectra at 500 K for all the structures of silicon mentioned in this paper.

300 K, whereas the calculations are at 500 K. Similar computed information on IR-active modes is shown in Fig. 13. Most structures have one or, in certain cases, two sharp peaks. The only noteworthy deviations from this feature are in cases of the orthorhombic structures, where there are greater widths compared to the other structures. This originates as a result of higher anharmonicity in the orthorhombic structures, quantitatively manifesting in higher values of $\Phi^{(3)}_{xyz}$, and since the FWHM is proportional to $|\Phi^{(3)}_{xyz}|^2$, the effect of anharmonicity will be much more pronounced in the spectra widths.

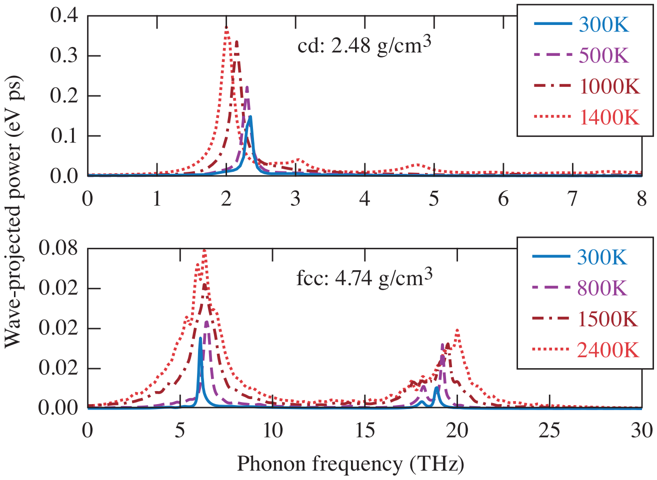

FIG. 14. Power spectra for (top) cd and (bottom) fcc along isochores, corresponding to densities of 2.48 and 4.74 g/cm^3, respectively, with increasing ionic and electronic temperatures ($T_\mathrm{i} = T_e$), highlighting the change in wave-projected power and contrasting shift in peaks.

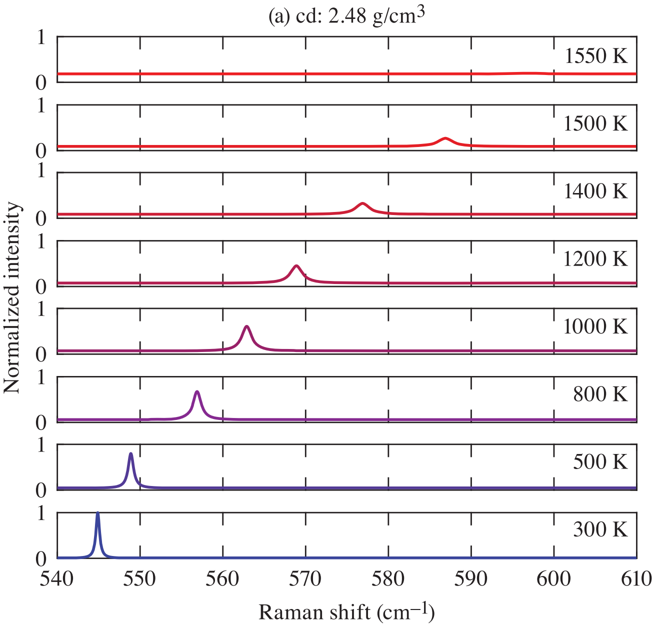

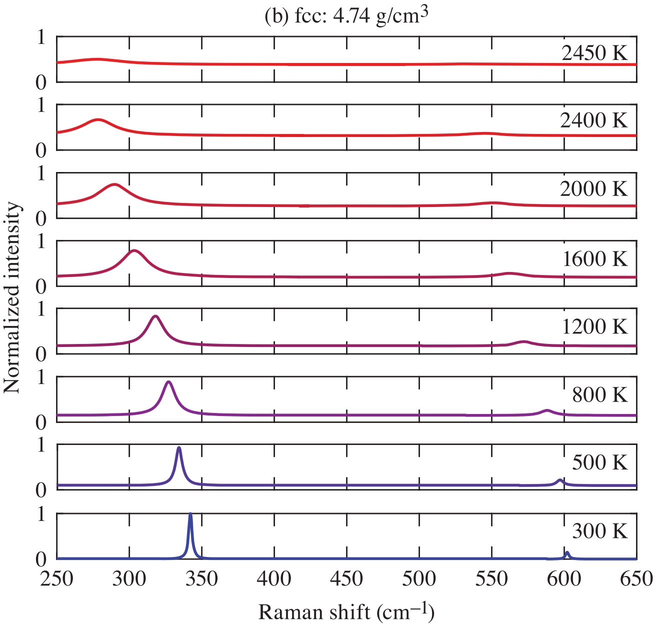

FIG. 15. Raman spectra of cd and fcc along isochores, corresponding to densities of (a) 2.48 g/cm^3 and (b) 4.74 g/cm^3, respectively, with increasing ionic and electronic temperatures ($T_\mathrm{i} = T_e$).

To calculate the effect of finite temperature on Raman shift, as discussed near the end of Sec. II D, the power spectra for cd and fcc were calculated using QMD and DYNAPHOPY. The results are shown in Fig. 14, where it is interesting to note that the first-peak phonon frequency for cd [Fig. 14 (top)] exhibits decreasing values with increasing temperature, whereas the maximum value of wave-projected power increases. This is in clear contrast to fcc [Fig. 14 (bottom)], where the phonon frequencies, generally speaking, increase along with the magnitude of the wave-projected power for all of the peaks. Qualitatively, this contrasting behavior can be attributed to the fact discussed earlier in Sec. III D that the cd isochore has a negative slope (corresponding to increasing density along an isobar), whereas the fcc isochore has a positive slope in the *P*-*T* space.

The change in Raman shift can be tracked as a function of temperature along an isochore; this can be used as another signature of melting. The cases are shown in Fig. 15, where the Raman shift wave number for cd increases from 545 to 587 cm^{-1}, accompanied by a broadening of the Lorentzian due to temperature effects. For fcc, the first Raman shift peak decreases from 342 to 278 cm^{-1} with increasing temperature. There is a second smaller peak as well, which disappears even earlier as temperature increases. The contrast between cd and fcc, concerning the direction of the movement of the peak in Raman shift, can be attributed to the different natures of their isochores, as discussed above. However, it is worth mentioning that the melting point (T_{melt}) predicted using this approach is intricately linked to *NVT*-QMD simulations, by virtue of the dependence on the power spectra for determining the FWHM and the Raman shift caused by thermal effects.

IV. CONCLUSIONS

In essence, we have built a holistic pressure-temperature (*P*-*T*) phase diagram, from first-principles calculations, including anharmonicity originating from finite-temperature ionic vibrations as well as changes in equilibrium lattice constants and axial ratios with temperature. In the lower-pressure solid regime, the dhcp structure has been predicted, corroborating an earlier computational prediction [47]. This particular structure emerges as a metastable prediction from evolutionary algorithm-based structure searches. In terms of pressure, extreme states of up to 4 TPa have been investigated. The results showed the existence of an anomalous sequence of fcc-bcc-sc transitions triggered by the movement of electrons from the interionic shared orbital space to the interstitial void; however, these high-pressure structures are still metallic solids. The melt curve has been calculated using *NVT*-QMD simulations; it is shown to have a negative slope for cd-liquid transitions. The remainder of the melt curve monotonically increases up to 4 TPa (corresponding to $T_{\mathrm{melt}} =\sim 26\,000$ K). In addition, the Raman and IR spectra of the different structures have been calculated and presented. We hope these results can facilitate experiments to probe the predicted unusual high-pressure states of silicon, which in turn may improve our understanding of materials under extreme conditions.

ACKNOWLEDGMENTS

This material is based upon work supported by the Department of Energy National Nuclear Security Administration under Award No. DE-NA0003856, the University of Rochester, and the New York State Energy Research and Development Authority.

---

[1] C. S. Zha, H. Liu, J. S. Tse, and R. J. Hemley, Phys. Rev. Lett. **119**, 075302 (2017).
[2] P. Dalladay-Simpson, R. T. Howie, and E. Gregoryanz, Nature **529**, 63 (2016).
[3] C. L. Guillaume, E. Gregoryanz, O. Degtyareva, M. I. McMahon, M. Hanfland, S. Evans, M. Guthrie, S. V. Sinogeikin, and H. K. Mao, Nat. Phys. **7**, 211 (2011).
[4] A. Lazicki, A. Dewaele, P. Loubeyre, and M. Mezouar, Phys. Rev. B **86**, 174118 (2012).
[5] A. A. Correa, L. X. Benedict, D. A. Young, E. Schwegler, and S. A. Bonev, Phys. Rev. B **78**, 024101 (2008).
[6] L. X. Benedict, K. P. Driver, S. Hamel, B. Militzer, T. Qi, A. A. Correa, A. Saul, and E. Schwegler, Phys. Rev. B **89**, 224109 (2014).
[7] K. P. Driver and B. Militzer, Phys. Rev. B **93**, 064101 (2016).
[8] M. Marqués, M. Santoro, C. L. Guillaume, F. A. Gorelli, J. Contreras-García, R. T. Howie, A. F. Goncharov, and E. Gregoryanz, Phys. Rev. B **83**, 184106 (2011).
[9] T. Sjostrom, S. Crockett, and S. Rudin, Phys. Rev. B **94**, 144101 (2016).
[10] D. Cebulla and R. Redmer, Phys. Rev. B **89**, 134107 (2014).
[11] I. Saika-Voivod, F. Sciortino, T. Grande, and P. H. Poole, Phys. Rev. E **70**, 061507 (2004).
[12] J. J. Fortney, S. H. Glenzer, M. Koenig, B. Militzer, D. Saumon, and D. Valencia, Phys. Plasmas **16**, 041003 (2009).
[13] V. N. Goncharov, T. C. Sangster, R. Betti, T. R. Boehly, M. J. Bonino, T. J. B. Collins, R. S. Craxton, J. A. Delettrez, D. H. Edgell, and R. Epstein *et al.*, Phys. Plasmas **21**, 056315 (2014).
[14] S. X. Hu, G. Fiksel, V. N. Goncharov, S. Skupsky, D. D. Meyerhofer, and V. A. Smalyuk, Phys. Rev. Lett. **108**, 195003 (2012).
[15] M. Lafon, R. Betti, K. S. Anderson, T. J. B. Collins, R. Epstein, P. W. McKenty, J. F. Myatt, A. Shvydky, and S. Skupsky, Phys. Plasmas **22**, 032703 (2015).
[16] A. Benuzzi-Mounaix, S. Mazevet, R. Ravasio, T. Vinci, A. Denoeud, M. Koenig, N. Amadou, E. Brambrink, F. Festa, and A. Levy *et al.*, Phys. Scr. **2014**, 014060 (2014).
[17] Y. Zhang, T. Sekine, H. He, Y. Yu, F. Liu, and M. Zhang, Geophys. Res. Lett. **41**, 4554 (2014).
[18] G. J. Cheng, M. Cai, D. Pirzada, M. J. F. Guinel, and M. G. Norton, J. Manuf. Sci. Eng. **130**, 011008 (2008).
[19] F. González-Cataldo, S. Davis, and G. Gutiérrez, Sci. Rep. **6**, 26537 (2016).
[20] R. Beyers, J. Appl. Phys. **56**, 147 (1984).
[21] V. V. Brazhkin, A. G. Lyapin, S. V. Popova, and R. N. Voloshin, Phys. Rev. B **51**, 7549 (1995).

[22] J. Lees and B. H. J. Williamson, Nature **208**, 278 (1965).

[23] A. Kubo, Y. Wang, C. E. Runge, T. Uchida, B. Kiefer, N. Nishiyama, and T. S. Duffy, J. Phys. Chem. Solids **69**, 2255 (2008).

[24] S. J. Turneaure, S. M. Sharma, and Y. M. Gupta, Phys. Rev. Lett. **121**, 135701 (2018).

[25] E. E. McBride, A. Krygier, A. Ehnes, E. Galtier, M. Harmand, Z. Konôpková, H. J. Lee, H. P. Liermann, B. Nagler, and A. Pelka *et al.*, Nat. Phys. **15**, 89 (2019).

[26] A. Mujica, A. Rubio, A. Muñoz, and R. J. Needs, Rev. Mod. Phys. **75**, 863 (2003).

[27] J. C. Jamieson, Science **139**, 762 (1963).

[28] F. P. Bundy, J. Chem. Phys. **41**, 3809 (1964).

[29] J. Z. Hu, L. D. Merkle, C. S. Menoni, and I. L. Spain, Phys. Rev. B **34**, 4679 (1986).

[30] H. Olijnyk, S. K. Sikka, and W. B. Holzapfel, Phys. Lett. A **103**, 137 (1984).

[31] J. Z. Hu and I. L. Spain, Solid State Commun. **51**, 263 (1984).

[32] A. Jayaraman, W. Klement, and G. C. Kennedy, Phys. Rev. **130**, 540 (1963).

[33] J. F. Cannon, J. Phys. Chem. Ref. Data **3**, 781 (1974).

[34] S. J. Duclos, Y. K. Vohra, and A. L. Ruoff, Phys. Rev. Lett. **58**, 775 (1987).

[35] M. I. McMahon, R. J. Nelmes, N. G. Wright, and D. R. Allan, Phys. Rev. B **50**, 739 (1994).

[36] M. Hanfland, U. Schwarz, K. Syassen, and K. Takemura, Phys. Rev. Lett. **82**, 1197 (1999).

[37] S. J. Duclos, Y. K. Vohra, and A. L. Ruoff, Phys. Rev. B **41**, 12021 (1990).

[38] R. Ahuja, O. Eriksson, and B. Johansson, Phys. Rev. B **60**, 14475 (1999).

[39] R. J. Needs and A. Mujica, Phys. Rev. B **51**, 9652 (1995).

[40] K. Gaál-Nagy and D. Strauch, Comput. Mater. Sci. **30**, 8 (2004).

[41] O. Strickson and E. Artacho, Phys. Rev. B **93**, 094107 (2016); S. X. Hu, B. Militzer, L. A. Collins, K. P. Driver, and J. D. Kress, *ibid.* **94**, 094109 (2016).

[42] S. X. Hu, R. Gao, Y. Ding, L. A. Collins, and J. D. Kress, Phys. Rev. E **95**, 043210 (2017).

[43] D. C. Swift, G. J. Ackland, A. Hauer, and G. A. Kyrala, Phys. Rev. B **64**, 214107 (2001).

[44] B. Militzer and K. P. Driver, Phys. Rev. Lett. **115**, 176403 (2015).

[45] W. Kohn and L. J. Sham, Phys. Rev. **140**, A1133 (1965).

[46] N. D. Mermin, Phys. Rev. **137**, A1441 (1965).

[47] C. Li, C. Wang, J. Han, L. Yan, B. Deng, and X. Liu, J. Mater. Sci. **53**, 7475 (2018).

[48] R. Paul, S. X. Hu, and V. V. Karasiev, Phys. Rev. Lett. **122**, 125701 (2019).

[49] A. B. Alchagirov, J. P. Perdew, J. C. Boettger, R. C. Albers, and C. Fiolhais, Phys. Rev. B **63**, 224115 (2001).

[50] A. Togo, F. Oba, and I. Tanaka, Phys. Rev. B **78**, 134106 (2008).

[51] A. Togo, L. Chaput, I. Tanaka, and G. Hug, Phys. Rev. B **81**, 174301 (2010).

[52] S. Baroni, S. de Gironcoli, A. Dal Corso, and P. Giannozzi, Rev. Mod. Phys. **73**, 515 (2001).

[53] D. Alfè, G. D. Price, and M. J. Gillan, Phys. Rev. B **64**, 045123 (2001).

[54] L. Vočadlo, I. G. Wood, M. J. Gillan, J. Brodholt, D. P. Dobson, G. D. Price, and D. Alfè, Phys. Earth Planet. Inter. **170**, 52 (2008).

[55] S. G. Moustafa, A. J. Schultz, E. Zurek, and D. A. Kofke, Phys. Rev. B **96**, 014117 (2017).

[56] V. A. Lubarda, Int. J. Solids Struct. **41**, 7377 (2004).

[57] A. Togo, L. Chaput, and I. Tanaka, Phys. Rev. B **91**, 094306 (2015).

[58] P. Brüesch, in *Phonons: Theory and Experiments II*, edited by P. Fulde, Springer Series in Solid-State Sciences Vol. 65 (Springer-Verlag, Berlin, 1986), pp. 97–101, 277(E)–278(E) (1986).

[59] D. Porezag and M. R. Pederson, Phys. Rev. B **54**, 7830 (1996).

[60] A. Carreras, A. Togo, and I. Tanaka, Comput. Phys. Commun. **221**, 221 (2017).

[61] A. R. Oganov and C. W. Glass, J. Phys. Chem. **124**, 244704 (2006).

[62] A. R. Oganov, A. O. Lyakhov, and M. Valle, Acc. Chem. Res. **44**, 227 (2011).

[63] A. O. Lyakhov, A. R. Oganov, H. T. Stokes, and Q. Zhu, Comput. Phys. Commun. **184**, 1172 (2013).

[64] G. Kresse and J. Hafner, Phys. Rev. B **47**, 558 (1993); **49**, 14251 (1994).

[65] G. Kresse and J. Furthmüller, Comput. Mater. Sci. **6**, 15 (1996).

[66] G. Kresse and J. Furthmüller, Phys. Rev. B **54**, 11169 (1996).

[67] J. P. Perdew, K. Burke, and M. Ernzerhof, Phys. Rev. Lett. **77**, 3865 (1996).

[68] J. P. Perdew, J. A. Chevary, S. H. Vosko, K. A. Jackson, M. R. Pederson, D. J. Singh, and C. Fiolhais, Phys. Rev. B **46**, 6671 (1992); **48**, 4978(E) (1993).

[69] P. E. Blöchl, Phys. Rev. B **50**, 17953 (1994).

[70] Q. Zhu, A. R. Oganov, and A. O. Lyakhov, CrystEngComm **14**, 3596 (2012).

[71] H. J. Monkhorst and J. D. Pack, Phys. Rev. B **13**, 5188 (1976).

[72] F. Birch, Phys. Rev. **71**, 809 (1947).

[73] E. R. Hernández and J. Íñiguez, Phys. Rev. Lett. **98**, 055501 (2007).

[74] L. Koči, R. Ahuja, L. Vitos, and U. Pinsook, Phys. Rev. B **77**, 132101 (2008).

[75] S. Nosé, Mol. Phys. **52**, 255 (1984).

[76] A. Baldereschi, Phys. Rev. B **7**, 5212 (1973).

[77] V. V. Kechin, J. Phys.: Condens. Matter **7**, 531 (1995).

[78] A. Neuhaus, Chimia **18**, 93 (1964).

[79] W. Kleber, Krist. Tech. **2**, 13 (1967).

[80] A. D. Becke and K. E. Edgecombe, J. Chem. Phys. **92**, 5397 (1990).

[81] J. B. Neaton and N. W. Ashcroft, Nature **400**, 141 (1999).

[82] A. R. Oganov, Y. Ma, Y. Xu, I. Errea, A. Bergara, and A. O. Lyakhov, Proc. Natl. Acad. Sci. USA **107**, 7646 (2010).

[83] J. H. Parker, D. W. Feldman, and M. Ashkin, Phys. Rev. **155**, 712 (1967).

[84] H. I. T. Hauge, M.A. Verheijen, S. Conesa-Boj, T. Etzelstorfer, M. Watzinger, D. Kriegner, I. Zardo, C. Fasolato, F. Capitani, and P. Postorino *et al.*, Nano Lett. **15**, 5855 (2015).